Long-term thermal performance analysis of a large-scale water pit thermal energy storage

Pan, Xinyu; Xiang, Yutong; Gao, Meng; Fan, Jianhua; Furbo, Simon; Wang, Dengjia; Xu, Chao

Published in:
Journal of Energy Storage

Link to article, DOI:
10.1016/j.est.2022.105001

Publication date:
2022

Document Version
Publisher's PDF, also known as Version of record

Journal of Energy Storage 52 (2022) 105001

Contents lists available at ScienceDirect

Journal of Energy Storage

journal homepage: www.elsevier.com/locate/est

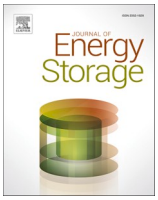

Research papers

Long-term thermal performance analysis of a large-scale water pit thermal energy storage

Xinyu Pan [a,b], Yutong Xiang [b], Meng Gao [b], Jianhua Fan [b,*], Simon Furbo [b], Dengjia Wang [c], Chao Xu [a]

[a] Key Laboratory of Power Station Energy Transfer Conversion and System of MOE, North China Electric Power University, Beijing 102206, China
[b] DTU Civil Engineering, Technical University of Denmark, Brovej, Building 118, 2800 Kgs. Lyngby, Denmark
[c] State Key Laboratory of Green Building in Western China, Xi'an University of Architecture and Technology, Xi'an, Shaanxi 710055, China

ARTICLE INFO

Keywords:
Water pit heat storage
Seasonal heat storage
Monitoring data analysis
Mathematical model
TRNSYS
Long term
Thermal performance analysis

ABSTRACT

Large-scale water pit thermal energy storage (PTES) promotes solar district heating (SDH) system as one of the most potential renewable applications for carbon neutrality. PTES needs vast investment and operates in a complicated system with numerous components, highlighting the need for a suitable simulation tool for tech-economic and feasibility investigations. This paper experimentally and theoretically investigated the long-term thermal performance of a 60,000 m^3 PTES in Dronninglund, Denmark. Five years measurements were analyzed to investigate the development of temperatures, heat flows, and thermal stratification in heat storage. A modified 2D model was proposed to calculate the thermal performance of the large-scale PTES based on the XST model in TRNSYS. The results showed that the developed model predicts well the storage temperatures and the heat flows. For one-year validation, the deviations of annual charged/discharged energy, internal energy content, and annual thermal loss between the model and the measurements were 2.0%/1.8%, 2.8% and 1.3%, respectively. The Dronninglund PTES showed 90.1% storage efficiency in the five-year investigation due to its high storage utilization cycle of 2.16. Even without any insulation on the sidewall and the bottom of the PTES, the average thermal loss from the two parts only accounted for 32.3% of total heat loss. Meanwhile, the soil region needed four years to stabilize. Approx. 24.4% of the heat loss in summer from the sidewall and the bottom is regained by the PTES in winter, when there is a low temperature in the heat storage. The findings of the paper serve as a good reference for designers and practitioners of water pit heat storage.

1. Introduction

Seasonal thermal energy storage (STES) enhances the rapid growth of solar district heating (SDH) toward decarbonizing the economy by eliminating the mismatch between supply and demand [1]. As reported by IEA, there were around 470 large-scale solar thermal systems (>350 kW_{th}, 500 m^2) in the world by the end of 2020, with 36% installed in the recent five years [2]. STES can significantly increase the penetration of solar energy in the energy system. Compared with the short-term TES system, the STES can increase the solar fraction of SDH systems from 25 to 50% or higher [3]. It can be predicted that the SDH system integrated with STES can become the primary source for substituting fossil fuel-based district heating plants [4].

Concerning STES for SDH systems, four main types exist in commercial applications, including tank TES (TTES), pit TES (PTES), borehole TES (BTES), and aquifer TES (ATES) [5]. Water becomes the dominant storage medium in STES due to its low cost, abundance, high heat capacity, and chemical stability [6]. At the same time, the TTES and PTES don't need special hydrogeological conditions as ATES does. Accordingly, the PTES and TTES are the most attractive and commercialized types. Yang et al. [7] compared different types of STES from different perspectives. The results depicted that the storage volume and efficiency have a positive impact. Although TTES has the best performance and less dependence on location, the storage type is expensive for a large-scale systems. The specific investment of PTES per unit storage volume decreases with an increase in the storage size. The PTES demonstrates better economic performance than other types when the size is larger than 10,000 m^3 [8]. In recent years, many attempts for large-scale PTES have been conducted in Europe. The storage volume has significantly increased, with a maximum storage volume of up to 200,000 m^3, which is so far the world's largest PTES [9].

* Corresponding author.
E-mail address: jif@byg.dtu.dk (J. Fan).

https://doi.org/10.1016/j.est.2022.105001
Received 7 February 2022; Received in revised form 1 May 2022; Accepted 27 May 2022

Nomenclature

Latin symbols

A	area, [m^2]
C	heat capacity, [J/K]
C_p	specific capacity, [J/(kg·K)]
E	energy content, [J]
F	conductive heat flow between adjacent layers, [W]
FB	heat flow through the boundary of the storage region, [W]
FCV	incoming/outcoming energy flows through adjacent layers, [W]
FR	heat flow through adjacent regions along the r-axis, [W]
FZ	heat flow through adjacent regions along the z-axis, [W]
h	enthalpy, [J/kg]
K	heat transfer ability, [W/K]
MIX	mix number, [−]
M_E	moment of energy, [J·m]
m	mass flow rate, [kg/m^3]
N	cycle number, [−]
Q	heat energy, [J]
$\dot{Q}$	heat energy flow. [W]
r	radius, [m]
R	diameter, [m]
R^2	coefficient of determination, [−]
th	thickness, [m]
T	temperature, [°C]
$TSCE$	temperature variation caused by direct water flow, [°C]
t	time, [s]
U	heat transfer coefficient, [W/(m^2·K)]
V	volume, [m^3]
$\dot{V}$	volume flowrate, [m^3/s]
z	vertical direction, [m]

Subscripts

0	initial
amb	ambient
cha	charge
discha	discharge
exp	experiment
gr	ground
max	maximum
mea	measurement
min	minimum
i, j	number of elements in 2D region
in	inlet flow
k	number of elements in 1D region
n	number of segments
out	outlet flow
r	R direction in cylindrical coordinate
ref	reference
s	soil
st	storage
th	thickness
tot	total
w	water
z	vertical direction

Greek symbols

ρ	density, [kg/m^3]
λ	thermal conductivity, [W/(m·K)]
η	efficiency, [−]
Δ	difference, [−]

Even if PTES is regarded as a promising approach for large-scale thermal energy storage, most of the projects were conducted only in a few countries. Approximately 75% of new SDH plants with PTES were installed in Denmark in the past ten years. The primary barrier is that the design seems challenging due to the various technical and economic differences [10–12]. The construction of large-scale PTES needs vast investment, highlighting the importance of modeling and design optimization of the PTES in order to guarantee its tech-economic feasibility. However, as STES is still in its early stage, current investigations focus on optimal design for small tanks. There were little efforts made for modeling large-scale thermal storages, especially for buried TES [11]. Therefore, it is essential to establish a suitable simulation tool for modeling and designing large-scale PTES.

The current simulation tools for PTES can be classified into two types: (a) computational fluid dynamic (CFD) for component-level modeling and (b) simplified 2D/3D numerical methods for system-level modeling [13]. CFD has been extensively adopted for detailed investigations of PTES. Almost all factors can be considered in CFD models, inclusive thermal properties of storage, design and geometry, surrounding soil conditions, and heat and mass transfer mechanism. Chang et al. [14,15] established a transient CFD model for a lab-scale PTES. Based on the experimental data, the effect of natural convection was investigated. Fan et al. [16] developed a CFD model to simulate the real-scale PTES in Marstal (75,000 m^3). Several typical operation conditions were considered in the investigations to study the thermal performance of both the storage and the surrounding soil region. Dahash et al. [17,18] employed a numerical model based on Comsol. The surrounding ground temperature was predicted by considering the effect of groundwater. The CFD models enable detailed investigations of the thermal performance of different PTESs minimizing the need for expensive experiments. Limited by the computational efforts, the sophisticated CFD models are suitable for short-time calculations [19]. But for PTES, some parameters vary in a few months. Generally, the pits need four to six years to reach steady condition [20]. On the other hand, as part of the SDH, simulation of the energy system should consider the effects of the related components, such as the solar field, heat pump, and the district heating (DH) network [21]. The current CFD simulations, as standing-alone models, are too complicated to build a compatible platform allowing calculation of system thermal performance.

The Engineering equation solver (EES) tools are widely used for system-level simulations. In such models, the PTES is simplified to reduce the computational efforts. Several researchers employed the lumped capacity models to calculate buried TES, which usually neglects the inner temperature distribution in the storage [22,23]. Kubiński et al. [24] established a dynamic model in Aspen HYSYS to calculate the entire thermal performance of the SDH system in Vojens, Denmark. The PTES was modeled as a fully-mixed tank, which differs far from reality. To investigate the internal heat transfer of PTES, Ochs et al. [25] developed a heat storage model in Matlab/Simulink coupling finite difference (FD) and finite element (FE). Simplifications were made on the geometry, material properties, and boundary conditions, which can be classified as a coarse model [19]. The TRNSYS environment is widely used to carry out system-level simulations due to its vast component library. Several coarse models were developed for buried TES, such as XST (Seasonal Ground Heat Storage), ICEPIT (Ice Pit thermal energy storage), and UGSTS (UnderGround Seasonal Thermal Storage) models [26]. Raab et al. [27] validated a 2795 m^3 water pit using the XST model in TRNSYS. The calculated results presented that the deviations between the measured and the calculated charging/discharging energy quantities are less than 5%. Bai et al. [28] proposed an under ground seasonal thermal energy storage (UGSTS) model based on TRNSYS to simulate a 3000 m^2 buried water pit. A good agreement was shown between the

measured and the simulated results with a relative difference lower than 2.8%. Recently, the TRNSYS model has been applied in large-scale PTES designs, such as in Gram [29]. Compared with small-scale PTES, large-scale PTES presents different characteristics affecting the simulation accuracy. Reiter et al. [30] simulated the Graz SDH plant with TRNSYS to predict the plant's output performance. The simulation results illustrated that it is technically feasible to build a large-scale SDH system with a PTES and a heat pump as proposed in the BIG Solar Graz concept. However, the simplified PTES with two buffers did not match the reality. Fan et al. [31] modified a TRNSYS model for the SDH system in Marstal, including a 75,000 m^3 PTES. In comparison with the measured results, the simulation could reflect the tendency of temperature developments in PTES but it failed to reproduce the thermal stratification in the pit, especially in May–August. Since many intricate factors affect the performance of SDH systems, the focus of the system-level simulations was mainly on optimization of the PTES capacity or the control strategy [32,33]. The lack of in-depth study could partly account for the inaccuracy of PTES simulation based on the TRNSYS model. In recent work, Xie et al. [34] simulated the PTES in Dronninglund with the ICEPIT model in TRNSYS. In the period of one year, the simulated results showed good agreements with the measurement in the energy flow of PTES and surrounding soil region. The influence of parameters, such as soil properties and inlet arrangement on the performance of PTES were elucidated. However, there were still issues remaining unsolved. For instance, the validity of the model was only examined for a duration of one year and the long-term behavior of the model remained unclarified. Since it typically takes four to six years for the surrounding soil of the PTES to reach stable conditions, investigations of the model accuracy in a longer duration of up to six years is necessary. Another drawback of the investigations is oversimplification of the initial condition of the PTES. A fictitious one year pre-simulation was used to achieve a better initial condition of the PTES and the soil around it. This oversimplification caused uncertainties in the calculation.

The literature review shows that it isn't easy to perform a coupled simulation considering both details of the PTES and the entire SDH system in a long-term period. Since there are only a few large-scale PTES in operation, it is difficult to validate and modify the current models due to the limited experimental data. With an aim to solve the remaining issues in the previous study (Xie et al. [34]), this work focuses on experimental and theoretical investigations of multi-year thermal performance of a 60,000 m^3 PTES in Dronninglund, Denmark. The XST model (Type 342) in TRNSYS was modified to correspond to the large-scale PTES of more than two inlet/outlet pipes. Measured data is used to provide more realistic initial conditions. Compared with five consecutive years of measured data, the proposed model will be validated using the key performance indicators, inclusive storage temperature, utilized energy, heat loss, thermal stratification index. The long-term performance of the model will be evaluated. This paper gives a comprehensive discussion on the degree of influence of different parameters and insights into the limitations and improvements of this model. It provides a reference for the planning and design of water pit heat storage.

2. Methodology

This section introduces the methodology adopted in the investigations, including the details of the PTES in Dronninglund, the experimental method, and the numerical model.

2.1. The experimental method

The Dronninglund SDH plant started to produce solar heat in May 2014. The plant was a part of “Sunstore 3 project” supported by the EUDP funding program of Denmark [35]. The project targeted producing 70% of the heat demand from renewable resources, of which 40% is solar energy. To achieve this, a large-scale solar collector field and a long-term STES are necessary. Fig. 1 presents an illustration of the entire system, inclusive of 35,573 m^2 solar collectors, a 60,000 m^3 (80 °C) water pit heat storage, and auxiliary heat devices (an absorption heat pump, two bio-oil boilers, a gas boiler, and four CHP gas engines). The forward/return temperatures of the heating network are 75/40 °C during non-heating seasons and 80/35 °C during heating seasons. The heat pump starts to work in winter and decreases the return water temperature to below 20 °C [36]. Therefore, the PTES is emptied before the start of the solar heating season, achieving a maximum heat capacity of the PTES and a higher utilization efficiency of the solar collectors.

In the Dronninglund SDH plant, the geometry of the PTES is an upside-down truncated pyramid stump with a slope of 26.6°, as shown in Fig. 2. The edge lengths of the top and the bottom surfaces are 90 m and 26 m, respectively [37]. Three inlet/outlet openings are installed in the top, the middle, and the bottom of the pit, switching between inlet and outlet modes according to the operation strategy of the system. Table 1 lists parameters of the PTES. Insulating materials are commonly used to cover the pit top surface to decrease heat loss from the PTES. In Dronninglund, the PTES utilizes a floating insulation cover with a 240 mm insulation layer. The primary material of the insulation layer is an 80 mm Nomalen 28 N insulation plate from NMC Termonova Oy. Furthermore, the Sunstore 3 report claimed that thermal loss from the lid accounts for the most of the PTES heat loss. The side and bottom surfaces of the PTES are only covered with 2.5 mm HDPE and 2 mm geotextile without insulation material.

The Dronninglund SDH plant is equipped with monitoring sensors connected to the supervisory control and data acquisition (SCADA) system. All data is recorded in the database with an interval of 10 min. For the PTES, temperatures, flow rates, heat flux, and humidity in the lid were measured, as illustrated in Fig. 2b. The sensor accuracy of the temperature is ±0.1 K, and the flow rate accuracy is ±2% [38]. Thermal stratification of the storage is measured with internal storage temperature sensors. Totally thirty-two temperature sensors with a distance of 0.5 m are divided into two vertical lines in the middle of the pit (position A and B). A heat flux sensor is installed in the middle of the insulation layer to observe the heat loss through the lid. Several sensors are placed in the technical room to monitor water's temperatures and volume flow rates through the three inlet/outlet pipes. The actual response time of the temperatures highly depends on the flowrate in the pipes due to the distance between the technical room and the water pit, which could be up to 20 min under low-flow rate conditions. Besides, four temperature sensors are set in the soil with a depth of 10, 15, 20, and 25 m below the water level of the storage (position C).

2.2. The numerical method

The finite difference method (FDM) is used in Type 342 to solve the heat flow equations. Time derivatives are approximated relying on the explicit FDM. The original model simulates heat storage in a water-filled tank, pond, or rock cavern with only one inlet/outlet couple [39]. For Dronninglund PTES connected with three inlet/outlet pipes, six couples of ports are needed to model all possible flow conditions. Therefore, a modified model increases the limits of ports for PTES in Dronninglund. In this paper, the simulation is carried out based on the following assumptions:

(1) Thermal conductivity and heat capacity are constant for water in the storage.
(2) In the storage, water at the same level has a uniform temperature due to thermal stratification. Natural convection in storage is modeled as a mixing procedure.
(3) In the soil region around the PTES, only heat conduction is considered. The influences of regional groundwater flow or natural convection in the surrounding soil are neglected.

The actual shape is transformed into a cylinder in Type 342. Fig. 3

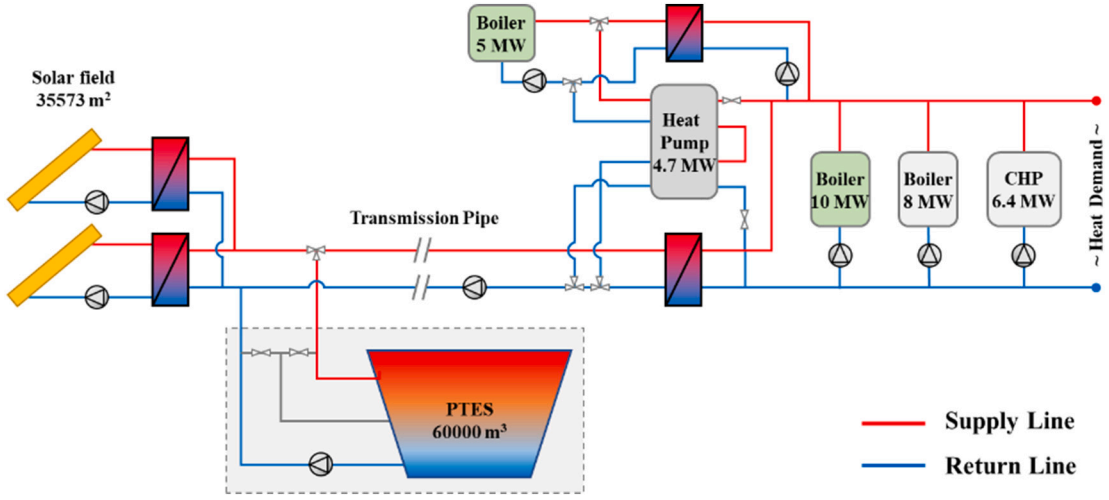

Fig. 1. Principle diagram of the SDH system with PTES in Dronninglund.

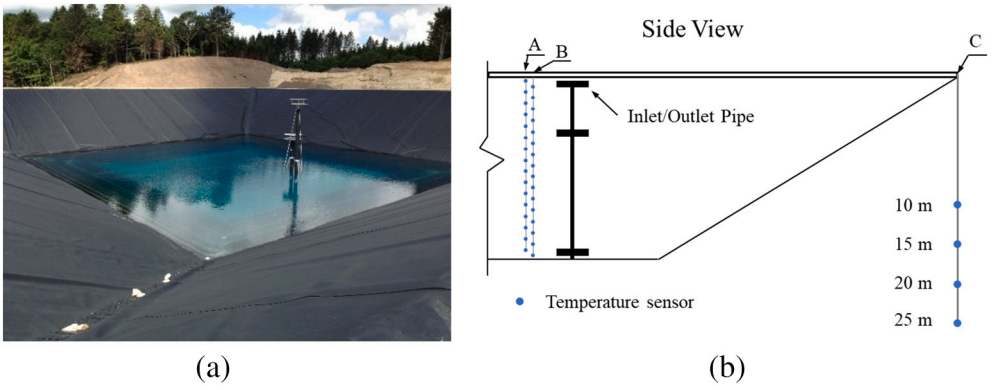

Fig. 2. Construction and geometrical illustration of the PTES in Dronninglund. (a) photo of the PTES during water filling, and (b) the position of the different sensors.

Table 1
Parameters of the PTES in Dronninglund [38].

Item	Description	Value	Unit
Geometry	Top edge length	90	m
	Bottom edge length	26	m
	Height	16	m
	Volume	59,285	m^3
Insulation of the lid	1: HDPE-Geomembrane	1.5	mm
	2: Hypernet CN-E	3	mm
	3: Nomalen	240	mm
	4: Hypernet HF-E	3	mm
	5: HDPE-Geomembrane	2	mm
Insulation of side and bottom	1: HDPE-Geomembrane	2.5	mm
	2: Hypernet HF-E	2	mm

shows the process of geometry transformation. It means that the surface areas of the storage in the model differ from the surface areas in reality, resulting in wrong thermal loss calculations. To deal with it, the differences in the surface areas could be compensated by modifying the heat transfer coefficient of the surfaces proportionally, as shown in Eq. (1) [34].

$$U_{\text{simulation}} = U_{\text{original}} \times \frac{A_{\text{original}}}{A_{\text{simulation}}} \tag{1}$$

where $U_{\text{simulation}}$ is the adopted heat transfer coefficient (W/(m^2·K)) in simulation, U_{original} is the real heat transfer coefficient (W/(m^2·K)), A_{original} is the real surface area (m^2), $A_{\text{simulation}}$ is the surface area after geometry transformation in the simulation (m^2). Table 2 lists the critical geometry parameters of the Dronninglund PTES.

2.2.1. The grid scheme

Type 342 simplifies the storage region into one dimension and the ground into two-dimension. The storage and soil region are typically divided into multi-nodes, as illustrated in Fig. 4. As the cylinder shape of the storage is axisymmetric, it is appropriate to calculate half of the region. The calculation algorithms depend on the mass and energy flow, heat conduction between nodes, and heat transfer through the walls. For the storage region, the geometry is divided into several layers (nodes) vertically [40]. It's assumed that each layer has a uniform temperature and the same volume. In this work, the original limit of the storage is modified for simulating large-scale storage, such as in Dronninglund. The storage is divided into 32 layers with the same height of 0.5 m as in the measurement. Three diffusers are installed in layers 1, 16, and 32, respectively. For the regions above the storage, the mesh relies on the thickness of the insulation lid. In the Dronninglund PTES, there is only the lid above the storage. A mesh with variable node size is generated for the soil regions beside and below the storage, whose node spacing decreases with an increase of the distance from the storage boundary.

2.2.2. Heat transfer in the storage region

As mentioned above, the temperatures in the storage volume are vertically stratified. The vertical thermal conductivity, forced convection via direct water flow, and heat transfer between the storage and the ground are taken into consideration in the model. The total mass flow

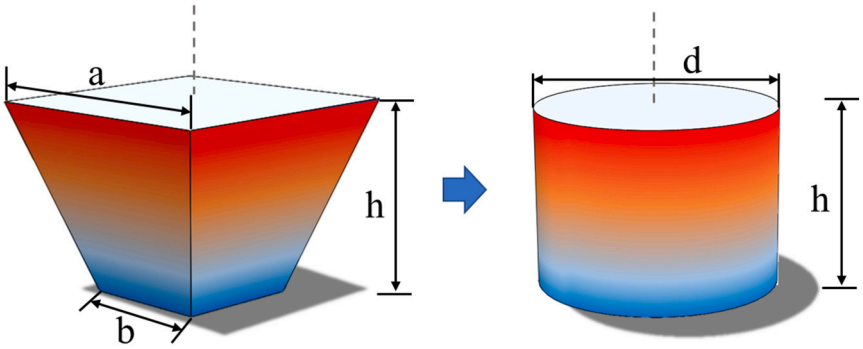

Fig. 3. Geometry transformation of PTES in the simulation.

Table 2
Geometry transformation of the PTES in Dronninglund.

Item	Reality	Simulation	Unit
Type	Reversed pyramid cone	Cylinder	–
Edges	a: 90 (Top), b: 26 (Bottom)	d: 34.3	m
Angle	26.6	90	°
Hight	16	16	m
Volume	59,285	59,285	m^3
Top surface	8100	3696	m^2
Side surface	8266	3448	m^2
Bottom surface	676	3696	m^2

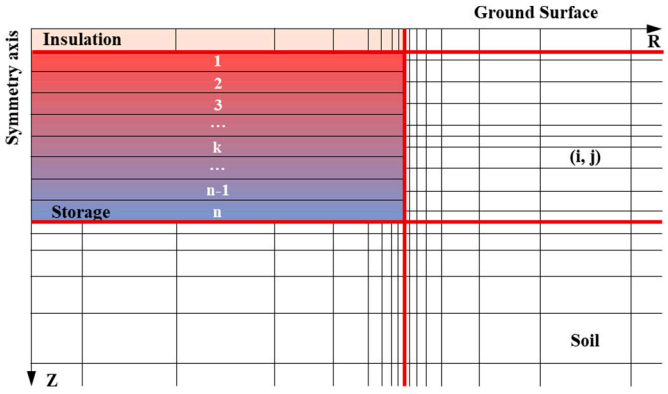

Fig. 4. Mesh-grid of the PTES in Dronninglund.

rate is equal to the sum of mass flow rates through all the openings, described as a steady-state continuity equation:

$$\sum \dot{m}_{\mathrm{in,tot}} = \sum \dot{m}_{\mathrm{out,tot}} = \rho \cdot \dot{V}_{\mathrm{w}} \tag{2}$$

The energy balance for a storage segment (k-th layer) is described as follows:

$$\frac{\partial E_{\mathrm{k}}(t)}{\partial t} = \sum \dot{m}_{\mathrm{k}} \cdot h_{\mathrm{k}} + \left(\dot{Q}_{z} - \dot{Q}_{z+\mathrm{dz}}\right) - \dot{Q}_{\mathrm{loss,k}} \tag{3}$$

where $\sum \dot{m}_{\mathrm{k}} \cdot h_{\mathrm{k}}$ denotes the input/output enthalpy flows, $\dot{Q}_{z} - \dot{Q}_{z+\mathrm{dz}}$ represents the conductive heat transfer between the adjacent layers, and $\dot{Q}_{\mathrm{loss,k}}$ defines thermal loss from the k-th layer. In this model, the energy balance of the storage can be further expressed as Eq. (4) based on the modified Euler method. The coefficients, f_1 and f_2 denote the exported heat transfer coefficient from the element (W/K) and imported heat into the segment (W), given in Eqs. (5) and (6), respectively.

$$V_{\mathrm{k}}\left(C_p \rho\right)_{\mathrm{st}} \frac{\partial T_{\mathrm{k}}}{\partial \tau} = f_1 T_{\mathrm{k}} + f_2 \tag{4}$$

$$f_1 = -K_{\mathrm{k}} - K_{\mathrm{k+1}} - A_{\mathrm{k}} U_{\mathrm{side}} \tag{5}$$

$$f_2 = \begin{cases} (K_{\mathrm{k}} + M_{\mathrm{oi}}) T_{\mathrm{k-1}} + (K_{\mathrm{k+1}} + M_{\mathrm{io}}) T_{\mathrm{k+1}} + A_{\mathrm{k}} U_{\mathrm{side}} T_{\mathrm{k}}^{\mathrm{st,gr}} + m C_p T_{\mathrm{inlet}}, & \text{layer with the inlet port} \\ (K_{\mathrm{k}} + M_{\mathrm{oi}}) T_{\mathrm{k-1}} + (K_{\mathrm{k+1}} + M_{\mathrm{io}}) T_{\mathrm{k+1}} + A_{\mathrm{k}} U_{\mathrm{side}} T_{\mathrm{k}}^{\mathrm{st,gr}}, & \text{layer without the inlet port} \end{cases} \tag{6}$$

where A_{k} is the touched area of the storage segment and the soil region, U_{side} is the heat transfer coefficient ($W/m^2 \cdot K$). K_{k} is the heat transferability between the storage layers (W/K), given by:

$$K_{\mathrm{k}} = \pi {R_{\mathrm{k}}}^2 \times \frac{\lambda_{\mathrm{st}}}{\Delta z_{\mathrm{k-1}}/2 + \Delta z_{\mathrm{k}}/2} \tag{7}$$

where R_{k} is the diameters of the storage layer, Δz_{k} denotes the node distance of the storage layers. In this model, the cylinder shape means they are constant for each storage layer. For forced convection, heat transfer depends on flow direction. M_{io} and M_{oi} are introduced to calculate the heat transfer between inlet and outlet due to water flow movement. According to the position of the inlet and outlet, M_{io} and M_{oi} could be described respectively:

$$\begin{cases} M_{\mathrm{io}} = mC_p; M_{\mathrm{oi}} = 0, & \text{Inlet port at lower z position} \\ M_{\mathrm{io}} = 0; M_{\mathrm{oi}} = -mC_p, & \text{Inlet port at higher z position} \end{cases} \tag{8}$$

Based on the FDM, the heat flows through the boundary of all storage layers can be calculated at the time t_0. They could be considered as constants during the following timestep (Δt). The energy balance for

each layer gives the changes in heat content during Δt. Therefore, new temperature for k-th layer at the time $t_0 + \Delta t$ can be given as follows:

$$T_{\mathrm{k}}(t_0+\Delta t) = T_{\mathrm{k}}(t_0) + \left(F_{\mathrm{k}}(t_0) - F_{\mathrm{k+1}}(t_0) + FB_{\mathrm{k}}(t_0) + FCV_{\mathrm{k}}(t_0)\right)/C_{\mathrm{st}}\cdot\Delta t + TSCE_{\mathrm{k}}(t_0) \tag{9}$$

where F represents the conductive heat flow between adjacent layers (W), FB denotes the heat flow from the boundary of the storage region (W), FCV means the incoming/outcoming energy flows through adjacent layers (W), C_{st} stands for the heat capacity of every layer (J/K), and $TSCE$ is introduced to reflect the temperature variation caused by direct water flow (°C). Eqs. (10)–(14) gives the detailed expressions.

$$F_{\mathrm{k}} = (T_{\mathrm{k-1}} - T_{\mathrm{k}})\cdot K_{\mathrm{k}} \tag{10}$$

$$FB_{\mathrm{k}} = \left(T_{\mathrm{k}} - T_k^s\right)\cdot A_{\mathrm{k}} U_{\mathrm{side}} \tag{11}$$

$$FCV_{\mathrm{k}} = M_{\mathrm{io}}(T_{\mathrm{k-1}} - T_{\mathrm{k}}) + M_{\mathrm{oi}}(T_{\mathrm{k}} - T_{\mathrm{k+1}}) \tag{12}$$

$$C_{\mathrm{st}} = \pi {R_{\mathrm{k}}}^2 \Delta z_{\mathrm{k}} \left(C_p\rho\right)_{\mathrm{st}} \tag{13}$$

$$TSCE_{\mathrm{k}} = (T_{\mathrm{inlet}} - T_{\mathrm{k}})V_{\mathrm{inlet}}/V_{\mathrm{k}} \tag{14}$$

2.2.3. Heat transfer in the soil/insulation region

The heat transfer that occurred in the soil region is assumed as pure thermal conduction and described as follows:

$$\left(C_{p,\mathrm{s}}\rho_{\mathrm{s}}\right)\frac{\partial T_{\mathrm{s}}(t)}{\partial t} = \nabla\cdot(\lambda_{\mathrm{s}}\nabla T_{\mathrm{s}}) \tag{15}$$

For the soil region (i, j), the new temperature at the time $t_0 + \Delta t$ can be given as follows referring to the calculation in the storage region:

$$T^{\mathrm{s}}_{\mathrm{i,j}}(t_0+\Delta t) = T^{\mathrm{s}}_{\mathrm{i,j}}(t_0) + \left(FZ_{\mathrm{i,j}}(t_0) - FZ_{\mathrm{i,j+1}}(t_0) + FR_{\mathrm{i,j}}(t_0) - FR_{\mathrm{i+1,j}}(t_0)\right)\Big/ C_{\mathrm{i,j}}\cdot\Delta t \tag{16}$$

where FZ and FR represents the heat flow (W) through adjacent regions along the z-axis and r-axis, respectively. C_{s} denotes the heat capacity of the soil region (J/K). Eqs. (17)–(22) represent the detailed expression for a central soil region.

$$FZ_{\mathrm{i,j}} = \left(T_{\mathrm{i,j-1}} - T_{\mathrm{i,j}}\right)\cdot K^z_{\mathrm{i,j}} \tag{17}$$

$$FR_{\mathrm{i,j}} = \left(T_{\mathrm{i-1,j}} - T_{\mathrm{i,j}}\right)\cdot K^r_{\mathrm{i,j}} \tag{18}$$

$$K^z_{\mathrm{i,j}} = A_{\mathrm{i,j}}\Big/\left(\frac{\Delta z_{\mathrm{j-1}}}{2\lambda_{\mathrm{i,j-1}}} + \frac{\Delta z_{\mathrm{j}}}{2\lambda_{\mathrm{i,j}}}\right) \tag{19}$$

$$K^r_{\mathrm{i,j}} = 2\pi\cdot\Delta z_{\mathrm{j}}\cdot\lambda^s_{\mathrm{i,j}}\cdot log(r_{\mathrm{i}}/r_{\mathrm{i-1}}) \tag{20}$$

Table 3
The reconstruction of the measured flow paths into dual ports for the model.

Flow path	Direction			Division	Equivalent port
	Top	Middle	Bottom	(Inlet, outlet)	
1	1	0	0	(M, T) + (B, T)	(3) + (5)
2	1	0	1	(M, T) + (M, B)	(3) + (4)
3	1	1	0	(B, T) + (B, M)	(5) + (6)
4	0	0	1	(T, B) + (M, B)	(2) + (4)
5	0	1	0	(T, M) + (B, M)	(1) + (6)
6	0	1	1	(T, M) + (T, B)	(1) + (2)

a) Direction: 1 means the pipe operates as an outlet, and 0 means inlet.
b) T means the top opening, M means the middle opening, B means the bottom opening.
c) Port: (1) (T, M), (2) (T, B), (3) (M, T), (4) (M, B), (5) (B, T), (6) (B, M).

$$C_{\mathrm{i,j}} = A_{i,j}\left(z_{\mathrm{i,j+1}} - z_{\mathrm{i,j}}\right)\left(C_p\rho\right)_{\mathrm{i,j}} \tag{21}$$

$$A_{\mathrm{i,j}} = \pi\left(R^2_{\mathrm{i,j+1}} - R^2_{\mathrm{i,j}}\right) \tag{22}$$

The boundary conditions of the soil or insulation regions are given in Eq. (23).

$$\begin{cases} K^r_{0,\mathrm{j}} = 0, K^r_{end,\mathrm{j}} = 0 \\ K^z_{\mathrm{i,1}} = 0, K^z_{\mathrm{i,end}} = 0 \\ T_{\mathrm{i,1}} = T_{\mathrm{amb}} \end{cases} \tag{23}$$

2.2.4. Parameters

The input parameters consist of the temperatures and flow rates of the three pipes connected to the PTES. The measurement shows that there are six possible flow paths through the PTES. One flow path could include two parallel inlets/outlets with different temperatures and flow rates. The type 342 model accepts only flow path with one inlet and one outlet. Therefore, a modified method is proposed to divide one measured flow path into two flow paths (dual ports) for the model. Water pits with three inlet/outlet pipes need six inlet/outlet ports to express the measured flow paths. Table 3 lists the possible flow paths and corresponding alternative ports. In this work, the original port limit has been increased to 12 for PTES simulation with multi-pipes (three or four).

According to the model simplification, the thermal property parameters of the PTES are constant in the simulation. The storage's volume heat capacity $(C_p\rho)_{\mathrm{st}}$ and thermal conductivity λ_{st} derive from the annual mean temperature in the period. For example, the $(C_p\rho)_{\mathrm{st}}$ and λ_{st} are 4148 kJ/(m^3·K) and 0.63 W/(m·K) respectively, for an average temperature of 39 °C in 2017. Referring to PlanEnergi's investigation [37], the soil thermal conductivity λ_{s} is 1.5 W/(m·K), and the volume heat capacity $(C_p\rho)_{\mathrm{s}}$ is 1800 kJ/(m^3·K). The thermal conductivity of new PE/PEX insulation is 0.04 W/(m·K). Considering the 30–50% degradation caused by high temperature and moisture, 0.06 W/(m·K) is finally used in the simulation [34]. Since there is no insulation covering the side and bottom surfaces of the storage, the heat transfer mainly includes water-side convection and thermal conduction in the liners.

The initial condition of the PTES in simulation has an apparent impact on the thermal performance of the PTES. One-year pre-simulation is a standard method conducted by many researchers to achieve a better initial condition [30]. The typical way is to repeat the simulation with the same inputs and use the results from the first year as the initial condition for the real calculation. This work uses the actual measured data, providing more realistic initial conditions for the PTES and the soil around it.

2.3. Performance assessment

The calculated thermal performance of the PTES is compared to the measured results. The charged/discharged energy can be derived directly from Eq. (23) [41]. For calculation of the measured energy, the fluid density (ρ, kg/m^3) and heat capacity (C_p, J/(kg·K)) can be obtained using the measured inlet/outlet temperatures, as shown in Eqs. (24) and (25) [42]. In the simulation, C_p is assumed to be constant, 4.18 kJ/(kg·K).

$$Q_{\mathrm{cha/discha}} = \left(\rho_{\mathrm{in}}C_{p,\mathrm{in}}T_{in} - \rho_{\mathrm{out}}C_{p,\mathrm{out}}T_{out}\right)\times V_{in}\times\Delta t \tag{23}$$

$$\rho = 1000.6 - 0.0128T^{1.76} \tag{24}$$

$$C_p = 4209.1 - 1.328T + 0.01432T^2 \tag{25}$$

Compared with the reference temperature T_{ref} (°C), the internal energy content of the PTES is defined in Eq. (26). In one year period, the internal energy change in the period (ΔQ_{st}) can be calculated by the difference of Q_{st} at the start and the end of the year.

$$Q_{st} = \sum_{k=1}^{k=n} \left(T_k - T_{ref}\right) \times C_p \times V_k \times \rho_k \tag{26}$$

The heat loss of the PTES includes three parts: the top, the side, and the bottom surface, as expressed in Eq. (27). In the simulation, the three heat losses can be calculated according to Eq. (11). For the measurement, it's hard to obtain the heat loss from the side and the bottom of the storage directly due to the lack of proper equipment measuring the underground heat flux. Only the lid has a heat flux sensor to record the top heat loss. The measurements can obtain the total heat loss based on the energy balance equation, see Eq. (28).

$$Q_{loss} = Q_{loss,top} + Q_{loss,side} + Q_{loss,bottom} \tag{27}$$

$$Q_{loss,mea} = \sum Q_{cha/discha} + \left(Q_{st,start} - Q_{st,end}\right) \tag{28}$$

The TES storage efficiency is one of the critical parameters to indicate the ability of the TES storage to recover the charged energy in a period. Due to the cooling of the PTES by the heat pump to a temperature below the DH return temperature, the modified storage efficiency is defined to consider the variation of internal energy change of the PTES, as shown in Eq. (29).

$$\eta_{st} = \left(Q_{discha} + \Delta Q_{st}\right)/Q_{cha} \tag{29}$$

Eq. (30) defines the maximum heat capacity of the PTES. $T_{st,max}$ and $T_{st,min}$ indicate the maximum and the minimum water temperatures of the storage in a period of time, respectively. The annual storage utilization cycle is defined in Eq. (31).

$$Q_{capacity,max} = C_p \rho V_{st} \left(T_{st,max} - T_{st,min}\right) \tag{30}$$

$$N_{cycle} = Q_{discha} / Q_{capacity,max} \tag{31}$$

Furthermore, thermal stratification plays a crucial role in PTES performance. Regarding thermal stratification, the MIX number expresses the degree of mixing by an indicator in the range of 0 to 1 [43]. It is defined by the moment of energy (M_E) as Eq. (31):

$$MIX = \frac{M_E^{Stratified} - M_E^{exp}}{M_E^{Stratified} - M_E^{fully-mixed}} \tag{31}$$

where $M_E^{Stratified}$ and $M_E^{fully-mixed}$ denote moment of energy for the perfectly stratified condition and the fully mixed condition, respectively. M_E^{exp} is the energy-momentum determined based on the measured or the calculated water temperatures in the pit. The MIX number evaluates the degree of thermal stratification, with a value of 1 for a fully mixed PTES and a value of 0 for a perfectly stratified PTES. M_E is expressed as follows.

$$M_E = \sum_{i=1}^{n} z_i \left(\rho_i V_i C_{p,i} T_i\right) \tag{32}$$

Table 4
Thermal performance of the PTES in Dronninglund in 2017.

Item	Measured	Simulated	Deviation
Maximum temperature	84.4 °C	86.6 °C	2.2 K
Minimum temperature	8.7 °C	8.9 °C	0.2 K
Storage heat capacity	5280 MWh	5309 MWh	0.5%
Charged energy	11,620 MWh	11,856 MWh	2.0%
Discharged energy	11,110 MWh	11,315 MWh	1.8%
Internal energy change	−610 MWh	−593 MWh	2.8%
Thermal loss	1120 MWh	1134 MWh	1.3%
Storage efficiency	90.4%	90.4%	0%
Storage cycle	2.10	2.13	1.4%

The measured energy values are rounded due to the sensor accuracy.

3. Experimental validation

Detailed measurement of the PTES was carried out in five consecutive years from 2015 to 2019. The measurement data in 2017 is used to validate the simulation model. Table 4 summarizes the comparison between the measured and the simulated results. Considering the measurement uncertainties, the measured values are rounded. The simulated inner temperatures represent 2.2 K and 0.2 K of differences in maximum and minimum PTES inner temperatures, respectively. Five energy indicators achieve no more than 2.8% of deviations in the simulation. Furthermore, the performance assessments obtained from the measurement and simulated data also maintain differences within 1.4%. The comparison shows an acceptable prediction accuracy of the model. A detailed comparison is given in the following section.

3.1. Water temperatures in the PTES

The simulated outlet temperatures of the three openings determine the accuracy of the energy flow calculations. Fig. 5 represents the outlet flow temperatures through the three openings in a year. The simulated results have a good agreement with the measurements, with temperature differences below 1.9 K at the start and end of the year. Notably, the measured temperatures have large fluctuations over the year, which is caused by delays of temperature measurement due to thermal inertia of the connection pipes. As mentioned above, the flows in the three inlet/outlet pipes frequently switch direction based on the control strategy of the PTES. It takes time for the fluid in the pipes to flow between the PTES and the technical room, therefore the temperature measurement is very inaccurate when there are frequent switches between discharging and charging modes. When there was change of operation mode, the sensors actually measured temperatures of water remaining in the connecting pipes, resulting in unrealistically outlet temperatures. The time lag could be up to 20 min for small water flows [34]. Remarkably, the middle pipe shows the most apparent fluctuations of outlet temperatures. The reason is that the middle pipe switches more frequently than the top and bottom pipes. As shown in Fig. 6b, the scattered dots in gray deviate a lot from the mainstream temperatures when there were changes of operation modes.

At the end of 2017, the measurement shows that there was an increase of the PTES internal energy of 610 MWh compared to the start of the year, as listed in Table 4. The simulated internal energy change is 17 MWh (2.8%) lower than the experimental result. The pit's mean temperature is a direct measure of the internal energy content of the PTES. Fig. 6 depicts the comparison between the measured and the simulated average temperatures. Overall, the simulated temperatures correspond well to the measured ones. The maximum temperature difference was 2.7 K in August. The visible error from August to September could result from simplifications of constant thermal properties and inaccurate measurements, which was also seen in the previous investigations of the authors using a PTES model with the shape of a pyramid cone [34]. Therefore, the geometry simplification of the PTES into a cylinder doesn't lead to extra deviation on internal energy content.

3.2. The charged and discharged energy

Table 5 shows a detailed comparison of the annual charged/discharged energies. In general, annual charged/discharged energy deviations are no more than 2%. Notably, the temperature measurement delay of the middle inlet/outlet pipe leads to significant differences when the middle pipe was used as the outlet. The simulated result shows a difference of 8.6% for the charging process and 22.2% for the

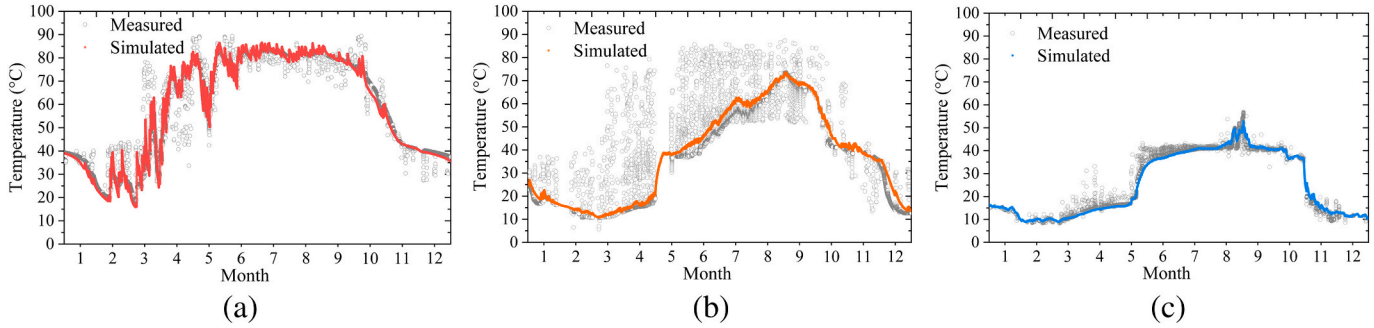

Fig. 5. The outlet temperatures of water flow through the three openings. (a) the top opening, (b) the middle opening, and (c) the bottom opening.

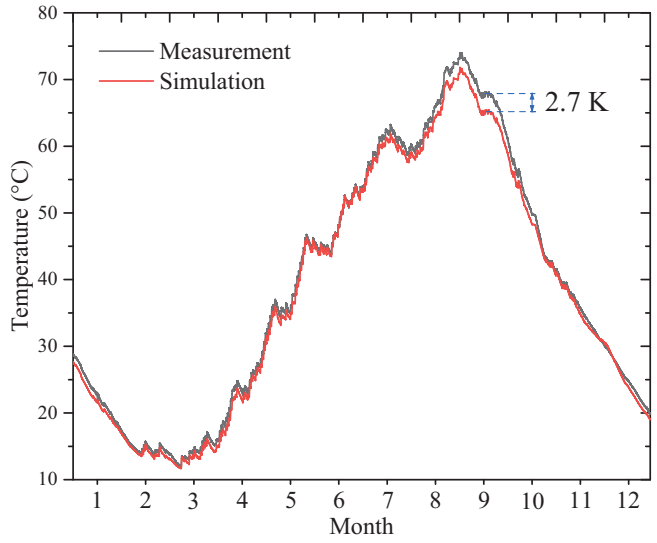

Fig. 6. The average temperature of the PTES in 2017.

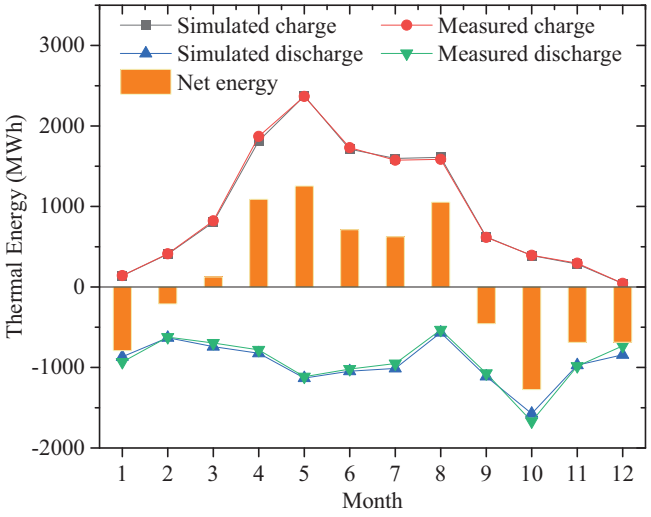

Fig. 7. Monthly charge/discharge energy in 2017.

Table 5
A detailed comparison of the charged and discharged energies for the three inlet/outlet pipes.

Conditions	Top/ Middle	Top/ Bottom	Middle/ Bottom	Total
Charging				
Measurement (MWh)	930	9180	1510	11620
Simulation (MWh)	1010	9335	1511	11856
Deviation (%)	8.6	1.6	0.1	2.0
R^2 (%)	84.1	99.9	99.7	94.6
Discharging				
Measurement (MWh)	1120	9140	850	11110
Simulation (MWh)	1126	9150	1039	11315
Deviation (%)	0.5	0.1	22.2	1.8
R^2 (%)	98.4	97.7	81.9	92.7

The measured energy values are rounded due to the sensor accuracy.

discharging process. Nevertheless, the other four conditions have good agreements with the measurements, with the R-square more than 97.7%.

Fig. 7 illustrates the monthly variations of the total charged/discharged energy. Even in summer, the PTES still output thermal energy to the DH network. The heat output kept a relatively stable level most of the year and reached the maximum in October. Therefore, the PTES serves as long-term storage and short-term storage simultaneously. The storage cycle was 2.13, higher than the storage cycle of approx. 1 for the other similar PTES [44].

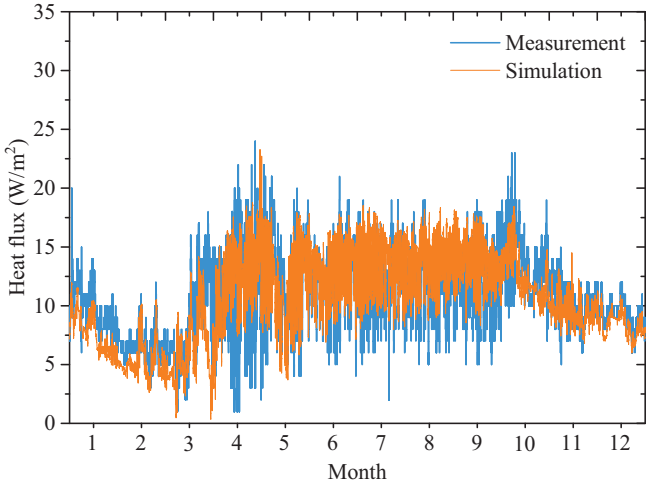

Fig. 8. Comparison of the measured and the simulated heat loss from the lid cover.

3.3. Heat loss

As the model considers a constant thermal conductivity and thickness for the lid insulation, the simulated heat flux through the lid has a close relationship with the water temperature of the upper storage layer and the ambient temperature. Fig. 8 demonstrates the yearly variations of the lid's measured and simulated thermal loss. There were individual

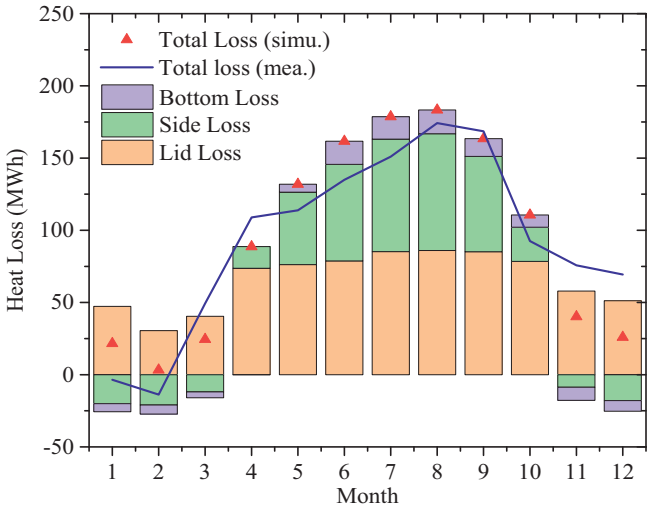

Fig. 9. Monthly heat loss from the top, the side, and the bottom surfaces of the PTES in 2017.

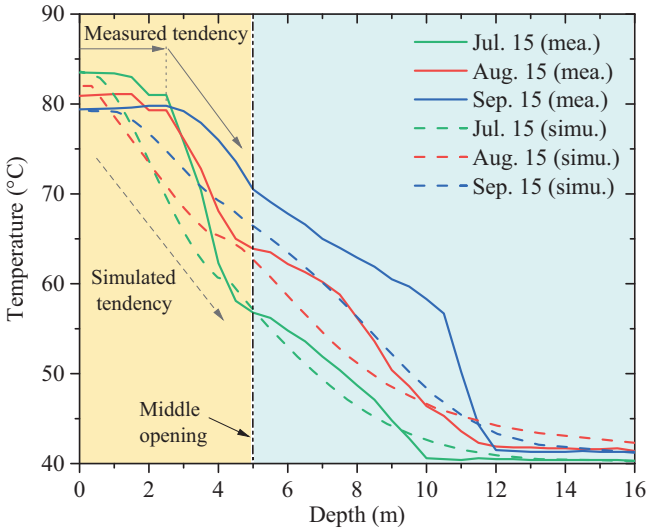

Fig. 11. Vertical temperature distribution of the PTES in summer 2017.

wrong heat loss measurements due to the failures of the heat flux meter. These wrong values have been filtered out. The total simulated lid loss is 791 MWh, which is only 1 MWh higher than the measurement. At the same time, both the experiment and the simulation present the same trend. In the discharging period, the heat pump decreases the storage temperature. From January to March, the upper layer temperature of the PTES decreased from 40 °C to 20 °C, resulting in a lower heat loss. A similar decrease of heat loss can also be seen from October to December. While from March to October, the heat loss increased significantly, due to an increase of the top layer temperature up to 80 °C. Variations of the ambient temperatures could explain the weekly fluctuations of heat loss.

As listed in Table 4, the measured and the simulated annual total heat loss of the PTES are 1120 and 1134 MWh, respectively. To further investigate the variation of thermal loss, Fig. 9 compares the monthly heat loss determined based on the simulation and the measurement. The simulated and measured results have a similar tendency, with the differences between 5.0 and 43.5 MWh. The highest and the lowest total heat loss occurred in August and February, respectively, strongly depending on the storage temperatures. The side loss illustrated the most apparent variety in a year. During the charging period, the side loss was very large, even approaching the top loss occasionally. Once the heat pump started to run in the discharging period, the side loss became negative because the storage temperature was lower than the temperature of the surrounding soil. The same applies to the bottom heat loss. For the side and the bottom surfaces, 112 MWh of heat transferred from the ground to the storage from November to March as a heat gain, which accounted for 24.6% of the heat loss from April to October. Therefore, the surrounding soil serves as extra heat storage, storing heat in Summer and releasing it in winter.

Furthermore, the accumulated side and bottom heat loss accounted for 26.1% and 3.7%, respectively. The principal thermal loss (70.8%) was from the lid. The simulated results prove that it's a good choice not to insulate the side and the bottom surface of the PTES based on cost and benefit analysis.

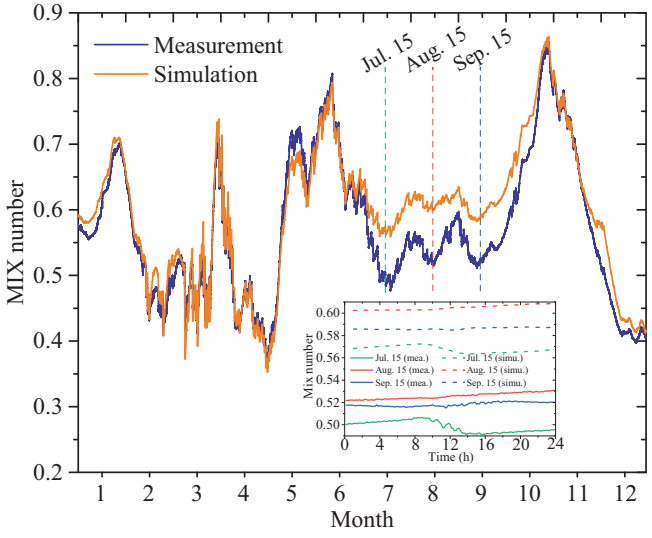

Fig. 10. The MIX number in Dronninglund PTES in 2017.

3.4. Thermal stratification

Thermal stratification in the PTES has a significant influence on the system's thermal performance. In order to preserve thermal stratification during charge and discharge, the PTES is equipped with three inlet/outlet openings at different heights: The top, the middle, and the bottom. A smart control strategy is used to lead the incoming water to the appropriate opening. However, thermal stratification in the PTES could be destroyed due to mixing induced by the incoming jet flow. Fig. 10 represents the MIX number in 2017. In our previous investigation, a noticeable deviation of the MIX number had appeared in summer [34]. The failures to consider mixing due to incoming jet flow and the limitation of the storage layer were blamed as the reasons for the difference. In this model, the natural convection is considered a mixing procedure when the upper layer temperature is lower than the adjacent layer below, and the layer number increases from 20 to 32. Compared with our previous work, the simulated MIX number can better depict a similar tendency of measured result than uncorrelated. At the same time, as shown in Fig. 11, the simulated upper and bottom temperatures match better the measured ones. The current model can accurately predict the effect of opening flow.

Nevertheless, the current model still overestimated mixing in the PTES in July–October. As shown in Fig. 11, the measured temperature distributions showed relative stability near the upper and more significant drop in the depth from 2 to 5 m. While the model only gave a continuous decreasing curve from the top to the middle. Therefore, the simulated M_E was smaller than the measured, resulting in a higher Mix number. The cause of the error could be the incapability of the model to consider natural convection in the PTES during the standby period. Previous authors' investigations on hot water heat storages showed that

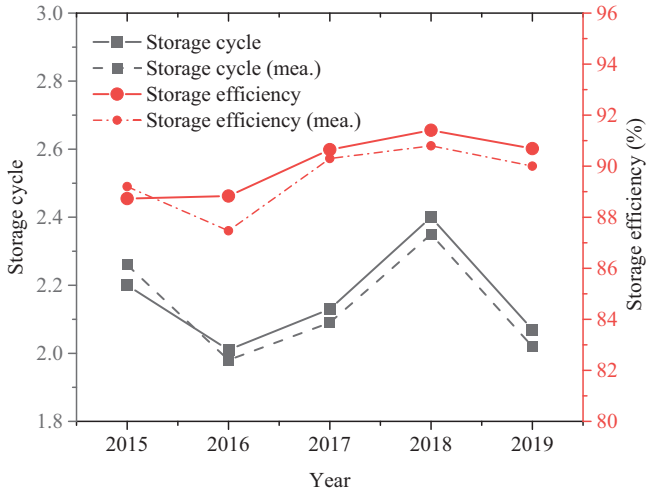

Fig. 12. Variations of the storage efficiency and the storage cycle of the PTES in 2015–2019.

natural convection caused by heat loss from the side surface helps establish thermal stratification [45]. Therefore, the current method is still not accurate enough in reproducing the temperature profile when natural convection is dominant. A temperature-dependent water thermal conductivity might be needed to estimate the inverse thermocline [18]. Except for the period from July to September, the simulated MIX number matched well with the measurement.

4. The long term thermal performance of the PTES

It typically takes several years for the soil around the PTES to reach thermal balance. Based on the validated model in TRNSYS and measured data in 2015–2019, the multi-year thermal performance of PTES can be investigated.

4.1. PTES thermal performance

Storage efficiency is a key performance indicator for PTES. Fig. 12 shows the measured and the TRNSYS predicted storage efficiency and storage cycle of the PTES in five years. For common STES, the storage cycle is around one due to the primary target for storing energy in summer and discharging it in winter [46]. Schmidt et al. mentioned that the Marstal PTES showed around 66% storage efficiencies in 2015 and 2016 with the storage cycle approaching 1.1, while the efficiency dropped to 39% in 2017 with the storage cycle decreasing to 0.7 [44,47]. The TRNSYS model predicts well the measured storage efficiency with a difference less than 2%. The storage cycle positively influences the storage efficiency, affecting the heat loss fraction in the discharged heat. For the Dronninglund PTES, the five-year average storage cycle reached 2.16, resulting in a higher storage efficiency of 90.1%. Since 2015 was the second operation year, the soil around the PTES was gradually heated up by the PTES. After 2016, the storage cycle becomes the dominant factor on storage efficiency. The maximum efficiency of 91.4% was achieved in 2018 due to the highest storage cycle of 2.35. Therefore, increasing the storage cycle is the primary way to utilize the PTES, resulting in a high storage efficiency. There is a good agreement between the measured and the TRNSYS predicted storage cycles.

Fig. 13 illustrates variations of the annual predicted heat loss from 2015 to 2019. Due to the hardware failures, the measured lid flux flow can not be obtained in the later two years. There is a relatively steady lid

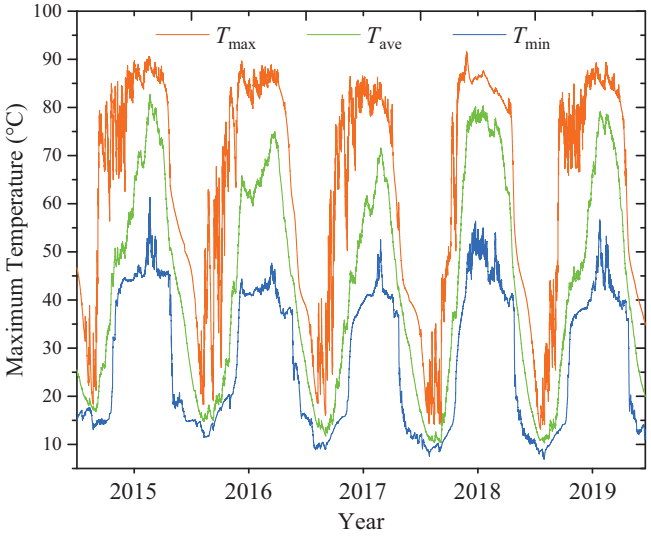

Fig. 14. Inner temperatures in the PTES from 2015 to 2019.

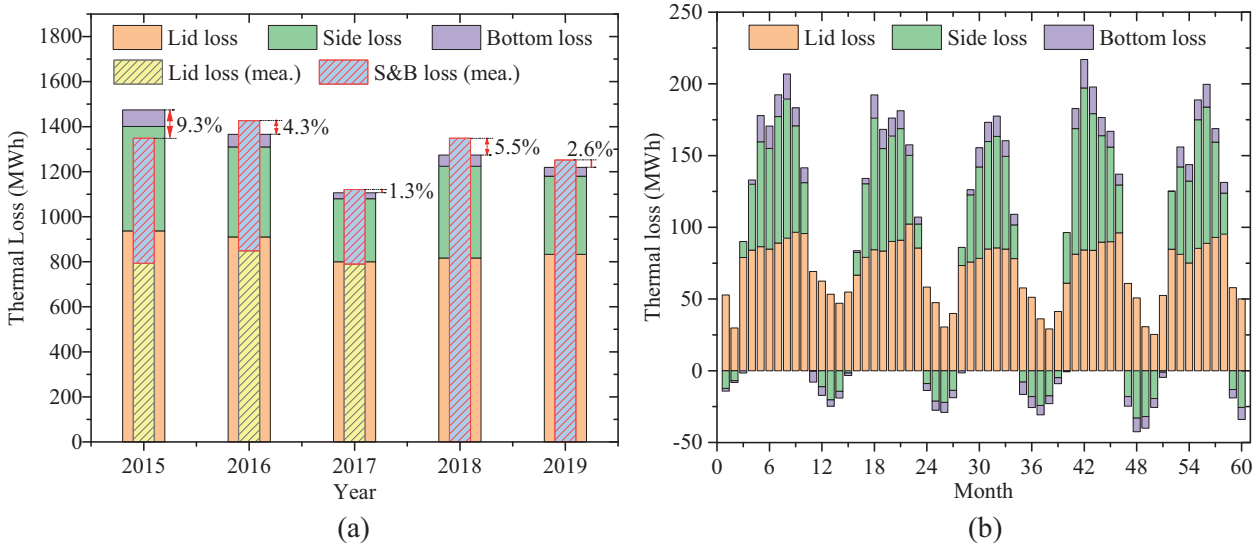

Fig. 13. The predicted thermal loss of the PTES in 2015–2019. (a) the yearly thermal loss, and (b) the monthly thermal loss.

heat loss in the range of 800 and 937 MWh, accounting for 63.5–72.3% of total heat loss. The constant thermal conductivity of the insulation material, 0.06 W/(m·K), was validated for 2017. Actually, the insulation performance has degraded with time. In 2015, the model overestimated the lid loss of 129 MWh due to the degradation of the insulation lid was not considered. In 2016, the deviation decreased to 5% because the corresponding thermal conductivity continued to approach in 2017. Therefore, a degradation calculation for the lid insulation is essential to include in the model for multi-year investigation. For the storage-soil boundary, the soil preheating significantly impacts the soil thermal properties. Compared with the other four years, the heat loss from the side and the bottom (S&B) surfaces in 2015 accounted for 36.5% of the total loss. After 2015, the proportion of storage-soil boundary loss decreased and fluctuated over the years. In 2017–2019, the average thermal loss from S&B was 383.8 MWh, accounting for 32.3% of the total heat loss. The multi-year simulation further justifies the design without S&B insulation in the Dronninglund PTES.

Moreover, Fig. 14 demonstrates the variations of the water temperature of the PTES. The average storage temperature depicts the internal energy content. In conjunction with Figs. 13b and 14, the thermal loss from S&B shows a similar tendency compared with the inner energy content changing of PTES. Usually, the PTES increases the internal energy content from March and arrives at the maximum in August or September. In 2018, the PTES maintained more than three months of high mean temperature above 75 °C. Accordingly, 587 MWh of positive heat loss from S&B occurred, accounting for 46.1% of yearly heat loss. As the heat pump was equipped in SDH plants, the minimum storage temperature can drop to around 10 °C in winter. Meanwhile, the upper water temperature can decrease to 15–20 °C, which is lower than the surrounding soil temperature. Unlike other times of the year when the water pit heat storage has much higher temperature, heat flows from the soil to the storage. In 2017–2019, the average negative heat loss was 124 MWh, accounting for 24.4% of positive heat loss from S&B. Although the charging energy from solar collectors varied in different years, the soil region can adjust the thermal energy through the storage boundary. In 2018, the negative heat loss was 131 MWh, leading to the yearly heat loss from S&B decreasing to 35.8%.

4.2. The soil around the PTES

The soil temperature is affected by many factors, including storage temperature, insulation, and soil conditions. Due to the simplification of the pyramidal-shaped PTES with a cylindrical one, the simulation result couldn't match the measurement directly. Fig. 15 illustrates the location difference of the measured and simulated temperature sensors. The sensor locations are transformed according to the distances between the storage boundary and the temperature sensors. Fig. 16 shows the variations of the soil temperatures in the depth of 10, 15, 20, and 25 m. The

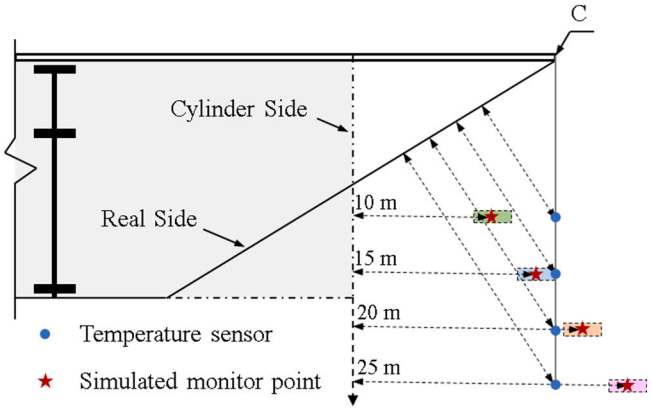

Fig. 15. Location transform of the soil temperature tensors in the simulation.

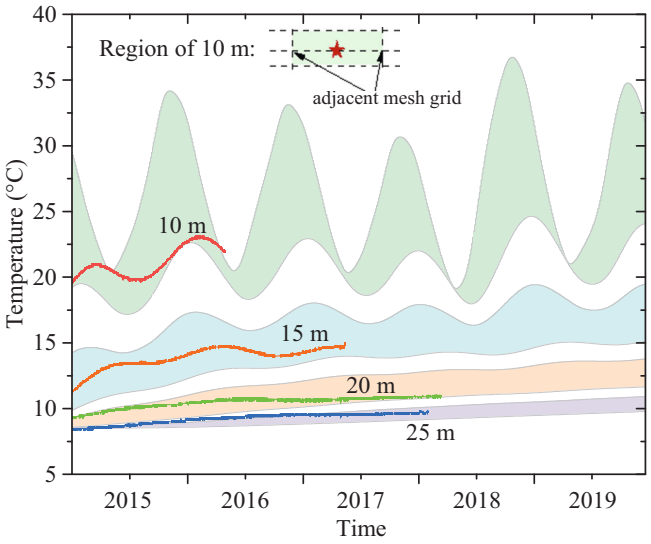

Fig. 16. Development of the soil temperatures with different depths in 2015–2019.

measured temperatures are present as the lines in magenta, orange, green, and blue, respectively. Due to hardware failures, only part of the measured data is successfully achieved [48]. Referring to Fig. 4, the soil temperature sensor locations are transformed into the mesh grid. Since there are uncertainties associated with the transformation, the corresponding simulated temperatures were presented as the "belt", meaning the bounding temperatures of the two horizontally adjacent mesh grids. Compared with the one-year simulation, the current model can reflect the development of long-term soil temperatures. Since the PTES started to operate in 2014, the results show that the soil thermal condition needed four years to stabilize. Due to the effect of ground water, the upper two soil temperatures show obviously seasonal variations. The closer the soil is to the storage, the larger the fluctuation of the soil temperature will be. While the deeper two temperatures increased in the first two years and then kept relatively stable. The soil temperature in the depth of 25 m was maintained at around 10 °C after four operation years. Although the measured soil temperature is mostly within the simulated temperature range, the simulation model overestimated the variation. Notably, in the depth of 10 m, the model predicts much larger fluctuations, which could be explained by the geometry simplification of the pit and inaccurate soil properties.

5. Conclusion

Experimental and theoretical investigations have been carried out to study the long-term thermal performance of the 60,000 m^3 water pit thermal energy storage in Dronninglund, Denmark. Detailed measurements of the PTES were performed in five consecutive years from 2015 to 2019. The measurement data was analyzed and used to validate the modified XST model of the PTES. The following conclusions could be drawn:

(1) The developed XST model can predict the actual thermal performance of the large-scale PTES. For 2017, the model calculated the charged and discharged energy with a 2.0% and 1.8% relative error, respectively. Except for the uncertainty caused by the time delay of temperature measurements in the middle inlet/outlet opening, the model predicted well the heat flows with R-squares of more than 97.7%.
(2) The modified XST model can predict well the MIX number in January–June and in October–December. However, a slight overestimation of the model is found in July–September. The

cause of the error could be the incapability of the model to consider natural convection in the PTES during standby period. Future improvement of the model should consider natural convection in the PTES and its influence on thermal stratification.

(3) Analysis of the long-term performance of the PTES shows that the storage cycle has a significant impact on storage efficiency. With the storage cycle increasing from 1.1 to 2.16, the storage efficiency improved from 66% to 90.1%.

(4) The heat loss through the cover accounted for 63.5–72.3% of the total thermal loss. For the PTES without insulation around the side and bottom surface, the average annual heat loss in 2017–2019 was 384 MWh, accounting for only 32.3% of the total heat loss. Equipped with the heat pump, the PTES can recover 24.4% of the heat loss from the surrounding soil region.

(5) It takes about four years for the soil region around the PTES to reach thermal balance. The fluctuations of the soil temperatures become larger with a decrease of the distance to the PTES boundary. The soil temperatures with a depth of 25 m or higher increased slowly over the years and then kept it around 10 °C due to the presence of underground water.

This work provides a developed model for the large-scale PTES and identified several remaining issues where further improvements are recommended. The finding of the paper serves as a good reference for designers and practitioners of water pit heat storages.

CRediT authorship contribution statement

Xinyu Pan: Writing, editing.
Yutong Xiang: Reviewing, proofreading.
Meng Gao: Reviewing and proofreading.
Jianhua Fan: Idea formulation, editing, fund raising.
Simon Furbo: Reviewing.
Dengjia Wang: Reviewing.
Chao Xu: reviewing.

Declaration of competing interest

The authors declare that they have no known competing financial interests or personal relationships that could have appeared to influence the work reported in this paper.

Acknowledgment

The research is jointly funded by the Danish Energy Agency EUDP project (no. 64020-2036), the EUDP project (no. 64020-2124) and the EUDP 2021-II project titled Participation in the IEA SHC Task on “Efficient Solar District Heating Systems”. We also thank Dronninglund Fjernvarme for provision of information and monitoring data of the water pit heat storage. Without their kind assistance and support, the research would not be possible.

References

[1] J. Xu, R.Z. Wang, Y. Li, A review of available technologies for seasonal thermal energy storage, Sol. Energy 103 (2014) 610–638, https://doi.org/10.1016/j.solener.2013.06.006.
[2] W. Weiss, M. Spörk-Dür, Solar Heat Worldwide, Austrian Research Institute AEE INTEC, Austria, 2021 https://www.iea-shc.org/solar-heat-worldwide-2021.
[3] Planenergi, Best Practice for Implementation And Operation of Large Sale Borehole And Pit Heat Thermal Storage, EUDP, Denmark, January 2019 https://www.solar-district-heating.eu/wp-content/uploads/2019/10/Best-practice-Br%C3%A6dstrup-Marstal-Dronninglund-and-Gram-003.pdf.
[4] Z. Tian, S. Zhang, J. Deng, J. Fan, J. Huang, W. Kong, et al., Large-scale solar district heating plants in Danish smart thermal grid: developments and recent trends, Energy Convers. Manag. 189 (2019) 67–80, https://doi.org/10.1016/j.enconman.2019.03.071.
[5] C. Bott, I. Dressel, P. Bayer, State-of-technology review of water-based closed seasonal thermal energy storage systems, Renew. Sustain. Energy Rev. 113 (2019), 109241, https://doi.org/10.1016/j.rser.2019.06.048.
[6] A.V. Novo, J.R. Bayon, D. Castro-Fresno, J. Rodriguez-Hernandez, Review of seasonal heat storage in large basins: water tanks and gravel–water pits, Appl. Energy 87 (2010) 390–397, https://doi.org/10.1016/j.apenergy.2009.06.033.
[7] T. Yang, W. Liu, G.J. Kramer, Q. Sun, Seasonal thermal energy storage: a techno-economic literature review, Renew. Sustain. Energy Rev. 139 (2021), 110732, https://doi.org/10.1016/j.rser.2021.110732.
[8] F. Ochs, A. Dahash, A. Tosatto, Janetti M. Bianchi, Techno-economic planning and construction of cost-effective large-scale hot water thermal energy storage for Renewable District heating systems, Renew. Energy 150 (2020) 1165–1177, https://doi.org/10.1016/j.renene.2019.11.017.
[9] H. Gadd, S. Werner, Thermal energy storage systems for district heating and cooling, in: Advances in Thermal Energy Storage Systems, Woodhead Publishing, 2021, pp. 625–638.
[10] R. Egging-Bratseth, H. Kauko, B.R. Knudsen, S.A. Bakke, A. Ettayebi, I.R. Haufe, Seasonal storage and demand side management in district heating systems with demand uncertainty, Appl. Energy 285 (2021), 116392, https://doi.org/10.1016/j.apenergy.2020.116392.
[11] A. Dahash, F. Ochs, M.B. Janetti, W. Streicher, Advances in seasonal thermal energy storage for solar district heating applications: a critical review on large-scale hot-water tank and pit thermal energy storage systems, Appl. Energy 239 (2019) 296–315, https://doi.org/10.1016/j.apenergy.2019.01.189.
[12] S. Furbo, J. Dragsted, B. Perers, E. Andersen, F. Bava, K.P. Nielsen, Yearly thermal performances of solar heating plants in Denmark – measured and calculated, Sol. Energy 159 (2018) 186–196, https://doi.org/10.1016/j.solener.2017.10.067.
[13] Y. Xiang, Z. Xie, S. Furbo, D. Wang, M. Gao, J. Fan, A comprehensive review on pit thermal energy storage: recent application, design and simulation approaches, J. Energy Storage (2022). Submitted for publication.
[14] C. Chang, Z. Wu, H. Navarro, C. Li, G. Leng, X. Li, et al., Comparative study of the transient natural convection in an underground water pit thermal storage, Appl. Energy 208 (2017) 1162–1173, https://doi.org/10.1016/j.apenergy.2017.09.036.
[15] C. Chang, B. Nie, G. Leng, C. Li, X. She, X. Peng, et al., Influences of the key characteristic parameters on the thermal performance of a water pit seasonal thermal storage, Energy Procedia 142 (2017) 495–500, https://doi.org/10.1016/j.egypro.2017.12.077.
[16] J. Fan, J. Huang, A. Chatzidiakos, S. Furbo, Experimental and theoretic investigations of thermal behavior of a seasonal water pit heat storage, in: Solar World Congress 2017 613, 2017.
[17] A. Dahash, M.B. Janetti, F. Ochs, Numerical analysis and evaluation of large-scale hot water tanks and pits in district heating systems, in: Building Simulation 2019 Conference, Rome (Italy), 02–04 September 2019, 2019, p. 614, https://www.solar-district-heating.eu/wp-content/uploads/2019/10/Best-practice-Br%C3%A6dstrup-Marstal-Dronninglund-and-Gram-003.pdf.
[18] A. Dahash, F. Ochs, A. Tosatto, W. Streicher, Toward efficient numerical modeling and analysis of large-scale thermal energy storage for renewable district heating, Appl. Energy 279 (2020), 115840, https://doi.org/10.1016/j.apenergy.2020.115840.
[19] F. Ochs, W. Heidemann, H. Müller-Steinhagen, Modeling large-scale seasonal thermal energy stores, in: Proceedings of Effstock, 2009, pp. 15–17.
[20] Y. Bai, M. Yang, J. Fan, X. Li, L. Chen, G. Yuan, et al., Influence of geometry on the thermal performance of water pit seasonal heat storages for solar district heating, Build. Simul. 579–99 (2021), https://doi.org/10.1007/s12273-020-0671-9616.
[21] K. Narula, F.D.O. Filho, J. Chambers, M.K. Patel, Simulation and comparative assessment of heating systems with tank thermal energy storage – a Swiss case study, J.Energy Storage 32 (2020), 101810, https://doi.org/10.1016/j.est.2020.101810.
[22] M. Jradi, C. Veje, B. Jørgensen, Performance analysis of a soil-based thermal energy storage system using solar-driven air-source heat pump for Danish buildings sector, Appl. Therm. Eng. 114 (2017) 360–373, https://doi.org/10.1016/j.applthermaleng.2016.12.005.
[23] H.F. Zhang, X.S. Ge, H. Ye, Modeling of a space heating and cooling system with seasonal energy storage, Energy 32 (2007) 51–58, https://doi.org/10.1016/j.energy.2006.02.007.
[24] K. Kubiński, Ł. Szabłowski, Dynamic model of solar heating plant with seasonal thermal energy storage, Renew. Energy 145 (2020) 2025–2033, https://doi.org/10.1016/j.renene.2019.07.120.
[25] F. Ochs, Large-scale thermal energy stores in district heating systems–simulation based optimization, in: EuroSun 2014: International Conference on Solar Energy And Buildings, 2014, p. 618.
[26] F. Ochs, Modelling Large-scale Thermal Energy Stores, Shaker Verlag, Stuttgart, 2009.
[27] S. Raab, D. Mangold, H. Müller-Steinhagen, Validation of a computer model for solar assisted district heating systems with seasonal hot water heat store, Sol. Energy 79 (2005) 531–543, https://doi.org/10.1016/j.solener.2004.10.014.
[28] Y. Bai, Z. Wang, J. Fan, M. Yang, X. Li, L. Chen, et al., Numerical and experimental study of an underground water pit for seasonal heat storage, Renew. Energy 150 (2020) 487–508, https://doi.org/10.1016/j.renene.2019.12.080.
[29] M.V. Jensen, Guidelines for design of seasonal pit heat storages, IEA SHC, 2014. http://task45.iea-shc.org/fact-sheets.
[30] P. Reiter, H. Poier, C. Holter, BIG solar Graz: solar district heating in Graz–500,000 m2 for 20% solar fraction, Energy Procedia 91 (2016) 578–584.
[31] J. Fan, J. Huang, O.L. Andersen, S. Furbo, Thermal performance analysis of a solar heating plant, in: Solar World Congress 627, 2017.

[32] P. Sorknæs, Simulation method for a pit seasonal thermal energy storage system with a heat pump in a district heating system, Energy 152 (2018) 533–538, https://doi.org/10.1016/j.energy.2018.03.152.
[33] M.H. Abokersh, M. Vallès, K. Saikia, L.F. Cabeza, D. Boer, Techno-economic analysis of control strategies for heat pumps integrated into solar district heating systems, J.Energy Storage 42 (2021), 103011, https://doi.org/10.1016/j.est.2021.103011.
[34] Z. Xie, Y. Xiang, D. Wang, O. Kusyy, W. Kong, S. Furbo, et al., Numerical investigations of long-term thermal performance of a large water pit heat storage, Sol. Energy 224 (2021) 808–822, https://doi.org/10.1016/j.solener.2021.06.027.
[35] PlanEnergi, Demonstration af stort solvarmeanlæg (Sunstore 3), EUDP, Denmark, 2009 https://www.energiteknologi.dk/projekter/demonstration-stort-solvarmeanlaeg-sunstore-3.
[36] D. Tschopp, Z. Tian, M. Berberich, J. Fan, B. Perers, S. Furbo, Large-scale solar thermal systems in leading countries: a review and comparative study of Denmark, China,Germany and Austria, Appl. Energy 270 (2020), 114997, https://doi.org/10.1016/j.apenergy.2020.114997.
[37] PlanEnergi, SUNSTORE 3 Fase 1: Projektering og udbud. https://energiforskning.dk/sites/energiforskning.dk/files/slutrapporter/slutrapport_incl._bilag_1_12042011_1824.pdf, 2011.
[38] PlanEnergi, SUNSTORE 3 Phase 2: Implementation, EUDP, Denmark, March 2015 https://planenergi.dk/wp-content/uploads/2018/05/26-Sunstore-3-Final-report.pdf.
[39] L. Mazzarella, S. Holst, Multi-flow stratified thermal storage model with full mixed layers, TRNSYS Version (1992). https://www.trnsys.de/static/d747464ad7627a47af6610ab89da64e9/Type_342_en.pdf.
[40] S. Scolan, S. Serra, S. Sochard, P. Delmas, J.-M. Reneaume, Dynamic optimization of the operation of a solar thermal plant, Sol. Energy 198 (2020) 643–657, https://doi.org/10.1016/j.solener.2020.01.076.
[41] E. Guelpa, V. Verda, Thermal energy storage in district heating and cooling systems: a review, Appl. Energy 252 (2019), 113474, https://doi.org/10.1016/j.apenergy.2019.113474.
[42] F. Bava, S. Furbo, A numerical model for pressure drop and flow distribution in a solar collector with U-connected absorber pipes, Sol. Energy 134 (2016) 264–272, https://doi.org/10.1016/j.solener.2016.05.012.
[43] M.Y. Haller, C.A. Cruickshank, W. Streicher, S.J. Harrison, E. Andersen, S. Furbo, Methods to determine stratification efficiency of thermal energy storage processes – review and theoretical comparison, Sol. Energy 83 (2009) 1847–1860, https://doi.org/10.1016/j.solener.2009.06.019.
[44] T. Schmidt, Marstal District Heating Monitoring Data Evaluation for the Years 2015-2017, Solites, Germany, 2019 https://www.solar-district-heating.eu/wp-content/uploads/2019/10/Marstal-evaluation-report-2015-2017_2019.05.28.pdf.
[45] J. Fan, S. Furbo, Thermal stratification in a hot water tank established by heat loss from the tank, Sol. Energy 86 (2012) 3460–3469, https://doi.org/10.1016/j.solener.2012.07.026.
[46] S. Koohi-Fayegh, M.A. Rosen, A review of energy storage types, applications and recent developments, J.Energy Storage 27 (2020), 101047, https://doi.org/10.1016/j.est.2019.101047.
[47] K. Narula, Filho F. De Oliveira, W. Villasmil, M.K. Patel, Simulation method for assessing hourly energy flows in district heating system with seasonal thermal energy storage, Renew. Energy 151 (2020) 1250–1268, https://doi.org/10.1016/j.renene.2019.11.121.
[48] C. Winterscheid, T. Schmidt, Dronninglund District Heating Monitoring Data Evaluation for the Years 2015–2017, Solites, Germany, 2019 https://www.solar-district-heating.eu/wp-content/uploads/2019/10/Dronninglund-evaluation-report-2015-2017_20190531.pdf.